Spring 2019

Coupling path visualization based on reciprocity theorem

Yang Zhong

Follow this and additional works at: https://scholarsmine.mst.edu/masters_theses

Part of the Electromagnetics and Photonics Commons

Department:

Recommended Citation

COUPLING PATH VISUALIZATION BASED ON RECIPROCITY THEOREM

by

YANG ZHONG

A THESIS

Presented to the Faculty of the Graduate School of the

MISSOURI UNIVERSITY OF SCIENCE AND TECHNOLOGY

In Partial Fulfillment of the Requirements for the Degree

MASTER OF SCIENCE IN ELECTRICAL ENGINEERING

2019

Approved by:

Chulsoon Hwang, Advisor
Jun Fan
David Pommerenke

ABSTRACT

A new method to visualize coupling path is proposed to help solve EMI problems. Based on the reciprocity theorem and the concept of reaction, coupling coefficient (CC) is defined to characterize coupling power density. For two-port networks, surface integral of CC can represent coupled voltage on the open-circuited port or coupled power on the loaded port. For dipole-moment based systems, surface integral of CC can represent coupled field components. The calculated CC should be a complex scalar at each point. By properly adjusting the excitation phases, the imaginary part of surface integral of CC will be zero and thus can be ignored. Also, the conservative property of the surface integral of CC makes it suitable for tracing the coupling path. Therefore, the coupling path visualization is fulfilled by plotting the real part of CC over the space between aggressor and victim. The calculated CC in rectangular coordinates has been applied in several full-wave simulations, and the coupling paths between aggressor and victim are clearly visualized. However, the limitation of using CC in rectangular coordinates is that the coupling paths around the aggressor or victim cannot be well characterized because the CC in rectangular coordinates is invalid in the region that is not between aggressor and victim. The CC in spherical coordinates is proposed to overcome this limitation. It also has been successfully applied in the coupling visualization for automotive intentional electromagnetic interference (IEMI) simulation.

ACKNOWLEDGMENTS

TABLE OF CONTENTS

LIST OF ILLUSTRATIONS

LIST OF TABLES

1. INTRODUCTION

Making the coupling path as inefficient as possible is a common approach to prevent unintentional interference. It might be easy to determine the coupling path between a few ideal behavior components. However, non-ideal behavior of components and hidden schematics may cause unanticipated emissions and make it difficult to identify the coupling path [1]. Since the modern electronic system is becoming more and more complicated, visualization will gradually become the inevitable and most straightforward method to characterize the coupling path.

Much effort has been given to identifying the coupling path through visualization [2]-[6]. A coupling path visualization method based on measurement has been introduced [2], but it can only be applied in specific cases where the transmitted signal is discontinuous and cannot be overlapped with the reflected signal. Moreover, this method requires knowledge of possible coupling paths in advance. In order to identify the coupling path without predetermination, the theoretical method is needed. The established theoretical methods include ray-tracing algorithms that use the rules of geometrical optics [3] or diffuse scattering [4] and the energy parcel and its trajectory concept that characterizes electromagnetic energy flow [5][6]. However, for the coupling issues, it is insufficient to only trace the energy flow of the transmitting sources. Even if Poynting vectors were found to be directed at the receiving structure, it is difficult to conclude that all energy represented by these vectors was finally coupled on the victim. For example, the part of energy reflected by the victim was not considered in these methods. Instead of the transmitting energy, the concept of coupled energy should be applied in the coupling path visualization. Rumsey

first gave the name "reaction" to represent the quantity that closely relates to the coupled energy between two sources [7]. The reaction theorem was then used in the mutual impedance calculation [8]. A coupling path visualization method using the concept of vector impedance density was proposed in [9]. This method overcame the limitation of plotting transmitter's Poynting vector. However, the physical meaning of the mutual impedance is not directly associated with the coupling path, and thus it is not straightforward for engineering insight. Besides, the mutual impedance concept requires an ideal current source connected to the aggressor port and open termination to the victim antenna, which is usually not the case in most practical problems. Therefore, a new coupling path visualization method is needed to characterize the coupling energy and be easily applied to engineering problems.

A new method to visualize the coupling path by using the concept of "reaction" and the reciprocity theorem is proposed. Instead of using the most widely used form of reciprocity by assuming the closed surface extends to infinity, closed surfaces that separate two sources are selected in the derivation. A complex scalar called the coupling coefficient (CC) is defined. The surface integral of CC can represent the coupled power on the load. The plotting of CC on each surface indicates the distribution of the coupling power density on that surface. By moving the surface over space, the coupling paths can be formed. Taking advantage that the defined parameters can be calculated in the commercial full-wave simulation tools, the coupling path can be easily visualized together with the simulation model. Thus, the proposed method can be widely used in solving EMC problems.

2. MATHEMATICAL FORMULATION

2.1. RECIPROCITY THEOREM

Assume that within a linear, isotropic medium, there are two sets of sources $\vec{J}_1, \vec{M}_1$ and $\vec{J}_2, \vec{M}_2$ that produce fields $\vec{E}_1, \vec{H}_1$ and $\vec{E}_2, \vec{H}_2$, respectively. For the fields to be valid, they must satisfy the following equation:

$$-\oiint_S \left(\vec{E}_1 \times \vec{H}_2 - \vec{E}_2 \times \vec{H}_1 \right) \cdot d\hat{s}' = \iiint_V \left(\vec{E}_1 \cdot \vec{J}_2 + \vec{H}_2 \cdot \vec{M}_1 - \vec{E}_2 \cdot \vec{J}_1 - \vec{H}_1 \cdot \vec{M}_2 \right) dv' \qquad (1)$$

Equation (1) is known as the Lorentz reciprocity theorem in integral form [10]. It is directly derived from Maxwell's equation without other assumptions [11]. In (1), V is the space enclosed by a surface S. There is no limitation on this closed surface. In particular, the left side of (1) is equal to zero when the surface S extends to the infinity.
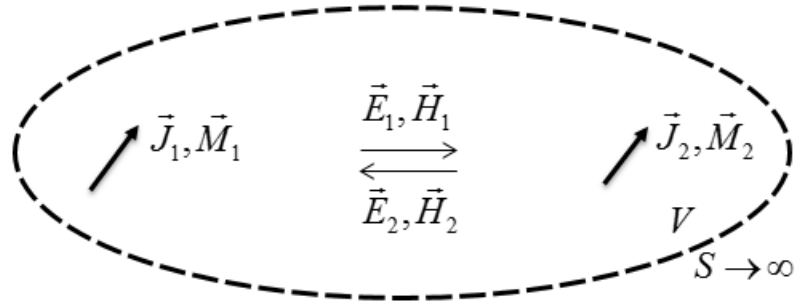
Figure 2.1. The closed surface covers the entire space

As shown in Figure 2.1, the surface S is far away from the sources. The propagation on the infinitely large surface S becomes plane wave. The left term of (1) can be written as

$$-\oiint_S \left(\vec{E}_1 \times \left(\hat{n} \times \frac{\vec{E}_2}{\eta} \right) - \vec{E}_2 \times \left(\hat{n} \times \frac{\vec{E}_1}{\eta} \right) \right) \cdot d\hat{s}' = 0 \tag{2}$$

In (2), η is the wave impedance, and $\hat{n}$ is the unit normal vector of the surface S, which is also perpendicular to $\vec{E}_1$ and $\vec{E}_2$. In this case, the reciprocity theorem can be simplified to

$$\iiint_V \left(\vec{E}_1 \cdot \vec{J}_2 - \vec{H}_1 \cdot \vec{M}_2 \right) dv' = \iiint_V \left(\vec{E}_2 \cdot \vec{J}_1 - \vec{H}_2 \cdot \vec{M}_1 \right) dv' \tag{3}$$

Equation (3) is the commonly used form in the radio frequency interference estimation [12-14].

2.2. REACTION

Reaction is the quantity represented by the integrals in the reciprocity theorem. Its definition is given by [7],

$$\langle 2,1 \rangle = \iiint_{V_1} \left(\vec{E}_2 \cdot \vec{J}_1 - \vec{H}_2 \cdot \vec{M}_1 \right) dv'$$

$$\langle 1,2 \rangle = \iiint_{V_2} \left(\vec{E}_1 \cdot \vec{J}_2 - \vec{H}_1 \cdot \vec{M}_2 \right) dv' \tag{4}$$

The symbol $\langle 2,1 \rangle$ represents the reaction from source 2 to source 1. In Figure 2.2 (a), the source $\vec{J}_1$ and $\vec{M}_1$ are enclosed by the surface S_1. Comparing the expression of $\langle 2,1 \rangle$ to the right side of (3), they are equivalent because there is no $\vec{J}_1$ and $\vec{M}_1$ outside of S_1. It is similar for the Figure 2.2 (b) and $\langle 2,1 \rangle$. According to the reciprocity theorem, the reactions between two sources are the same,

$$\langle 1,2 \rangle = \langle 2,1 \rangle \tag{5}$$
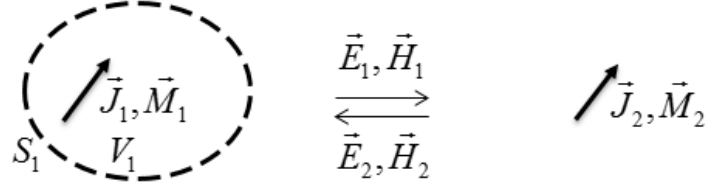
(a) The closed surface only covers the source 1
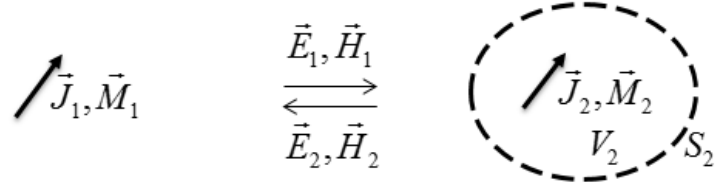
(b) The closed surface only covers the source 2

Figure 2.2. The closed surface that separates two sources

2.3. COUPLING COEFFICIENT

Figure 2.3 shows the special case of the Figure 2.2. The closed surfaces S_1 and S_2 become infinite large planes, which are equivalent to the original closed surfaces. For the S_1 and V_1 in Figure 2.3 (a), the reciprocity (1) can be written as

$$\iint_{S_1 \to \infty} \left[\left(\vec{E}_1 \times \vec{H}_2 - \vec{E}_2 \times \vec{H}_1 \right) \cdot \hat{n}_1 \right] ds' = \langle 2,1 \rangle \tag{6}$$

In Equation (6), $\hat{n}_1$ is the unit normal vector of the surface S_1. Similarly, for the S_2 and V_2 in Figure 2.3 (b), the reciprocity gives that

$$- \iint_{S_2 \to \infty} \left[\left(\vec{E}_1 \times \vec{H}_2 - \vec{E}_2 \times \vec{H}_1 \right) \cdot \hat{n}_2 \right] ds' = \langle 1,2 \rangle \tag{7}$$

$S_1 \to \infty$

$\hat{n}_1$

$\vec{J}_1, \vec{M}_1$

$\vec{J}_2, \vec{M}_2$

V_1
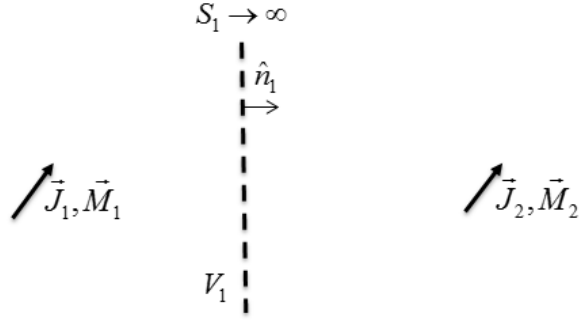
(a) A special surface that enclosed source 1

$S_2 \to \infty$

$\hat{n}_2$

$\vec{J}_1, \vec{M}_1$

$\vec{J}_2, \vec{M}_2$

V_2
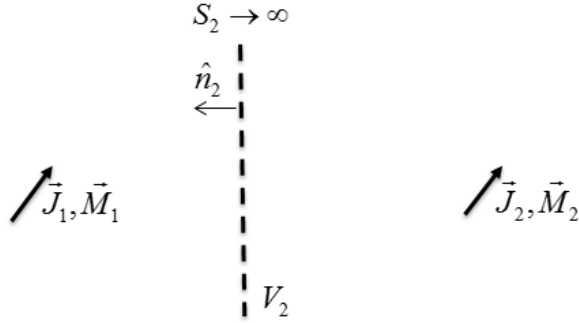
(b) A special surface that enclosed source 2

Figure 2.3. Infinite large plane surface that separates two sources

In Equation (7), $\hat{n}_2$ is the unit normal vector of the surface S_2. If S_1 and S_2 are overlapped, $\hat{n}_2$ will become $-\hat{n}_1$. Comparing (6) and (7), the reactions still satisfy the relationship in (5). In general, for any infinitely large plane S that separates $\vec{J}_1, \vec{M}_1$ and $\vec{J}_2, \vec{M}_2$, let the unit vector be perpendicular to the plane and directed to the right side as the unit normal vector $\hat{n}$ of S. The coupling coefficient (CC) is then defined as the quantity under the surface integral in (6) and (7) as

$$CC = \left(\vec{E}_1 \times \vec{H}_2 - \vec{E}_2 \times \vec{H}_1 \right) \cdot \hat{n} \qquad (8)$$

CC is a complex scalar and its value usually varies from locations. The unit of CC is W/m^2. The physical meaning of this parameter will be addressed in next section. Substituting (8) into (6) and (7), the reaction can be represented by the integral of CC over the infinitely large plane S that separates the two sources:

$$\langle 1,2 \rangle = \langle 2,1 \rangle = \iint\limits_{S \to \infty} CCds'$$

(9)

3. PHYSICAL INSIGHT

3.1. OPEN CIRCUIT VOLTAGE

As shown in Figure 3.1, there are two antennas in the two-ports network. In order to obtain the fields generated by antenna 1 and 2, the forward problem and the reverse problem are conducted respectively.
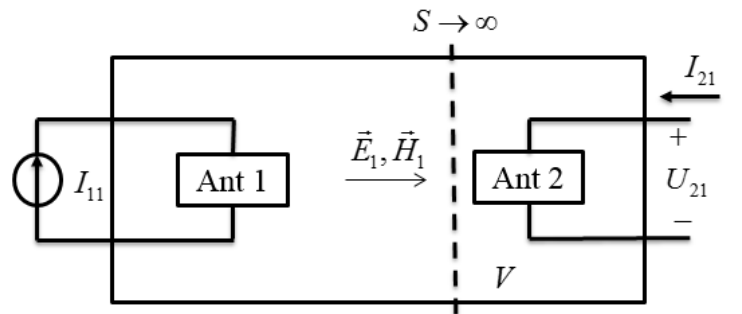
(a) The forward problem
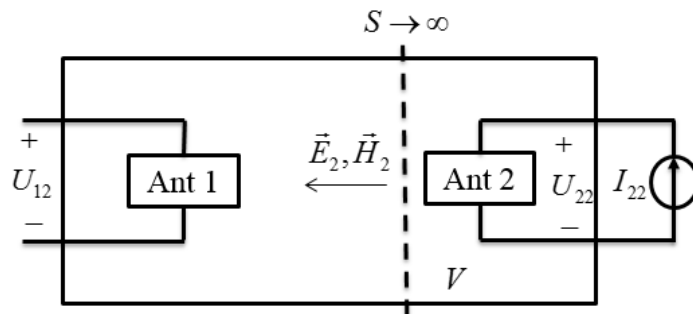
(b) The reverse problem

Figure 3.1. Coupling between the open circuit antennas

In the forward problem, antenna 1 is excited by current source I_{11} and generates fields $\vec{E}_1, \vec{H}_1$. The open circuit voltage on antenna 2 is represented by U_{21} , and the coupled

current I_{21} is zero. In the reverse problem, port 1 is open. Current source I_{22} feeds antenna

2 and creates fields $\vec{E}_2, \vec{H}_2$. The reaction on port 2 can also be expressed in terms of

voltages and currents by following the procedure in [7]:

$$\langle 1,2 \rangle = \iiint_V \left(\vec{E}_1 \cdot \vec{J}_2 - \vec{H}_1 \cdot \vec{M}_2 \right) dv = U_{21} I_{22} + U_{22} I_{21} = U_{21} I_{22} \tag{10}$$

Furthermore, if the unit current generator I_{22} =1 A is used in the reverse problem,

the open circuit voltage in the forward problem can be represented by the reaction or the

surface integral of coupling coefficient:

$$U_{21} = \langle 1,2 \rangle = \iint_{S \to \infty} CCds' \tag{11}$$

The mutual impedance Z_{21} between two antennas is defined as the ratio of voltage

U_{21} and current I_{11} when the victim antenna is open circuited where current I_{21} is zero:

$$Z_{21} = \frac{U_{21}}{I_{11}} \bigg|_{I_{21}=0} = \frac{1}{I_{11} I_{22}} \iint_{S \to \infty} CCds' \tag{12}$$
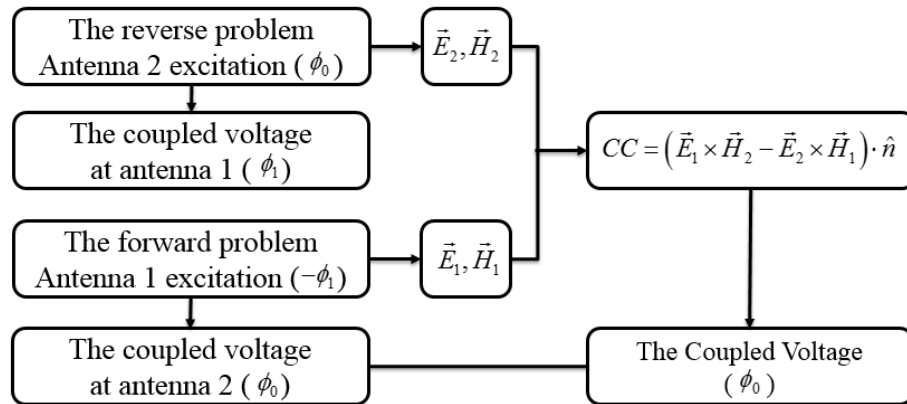
Figure 3.2. The procedure to avoid imaginary part of the coupled voltage
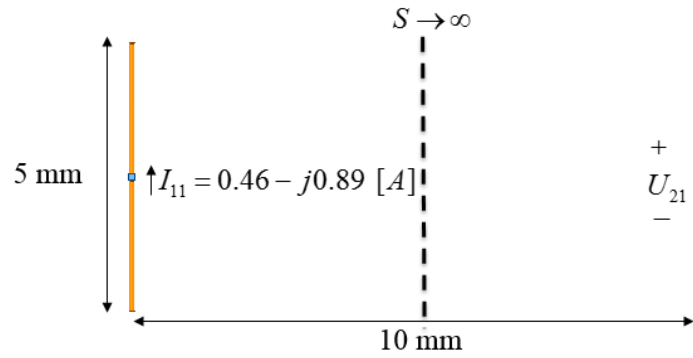
(a) The forward problem
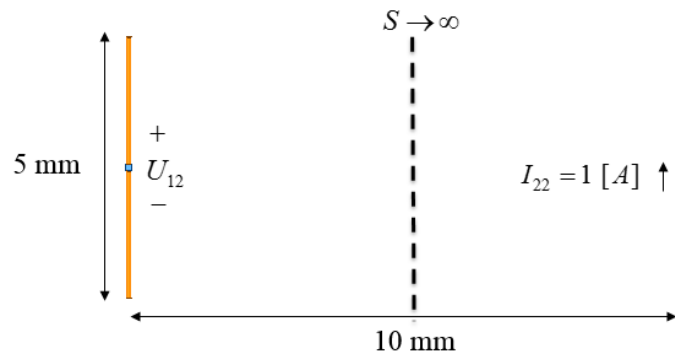
(b) The reverse problem

Figure 3.3. Two half-wavelength dipole antennas with open circuit ports

The procedure of eliminating the imaginary part is illustrated in Figure 3.2. A full-wave simulation model was used to validate (11). In Figure 3.3, two half-wavelength dipole antennas were placed 10 mm away from each other. The excitation frequency was 30 GHz. In the forward problem, the current source I_{11} =1 A fed the left-side antenna. The open circuit voltage U_{21} was measured to be 10.25+j18.06 V. The phase difference between U_{21} and I_{11} was 60.42 degrees. By adjusting the excitation phase to be −60.42 degrees in the forward problem, the coupled voltage became a pure real value U_{21} = 20.76 V. By using the definition (8), the coupling coefficients over the whole space can be calculated.

Figure 3.4 shows the real part of CC on the large plane in the middle of the two antennas. Its surface integral was equal to 20.76 V, numerically the same as the coupled voltage U_{21} in the forward problem. The imaginary part of CC was ignored because its surface integral equaled zero after using the phase adjustment. Otherwise, the complex CC needs to be investigated because the coupled voltage consists of both real and imaginary parts. For the open circuit case, the surface integral of CC represents the product of the inverse current and the forward coupled voltage. By setting the inverse current source to be 1 A, the surface integral of CC is equivalent to the coupled voltage.
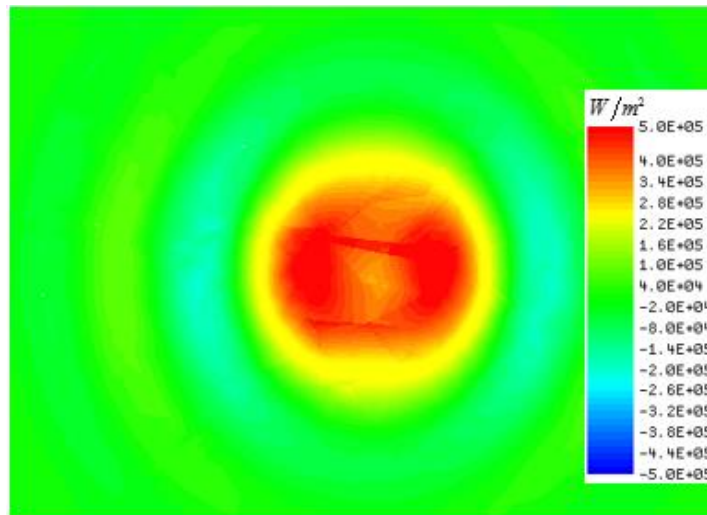
Figure 3.4. The real part of CC on a large plane

3.2. COUPLED POWER ON THE LOAD

In most applications, the victim antenna will be terminated with a load Z_L as shown in Figure 3.5 (a). To distinguish from the open circuit case, the notations in Figure 3.5 are changed. The superscript "fwd" and "rev" indicate the problem types. The subscript "1"

and "2" refer to the port numbers. The coupled voltage U_2^{fwd} on the load is no longer equal to the coupled voltage U_{21} on the open circuited port.
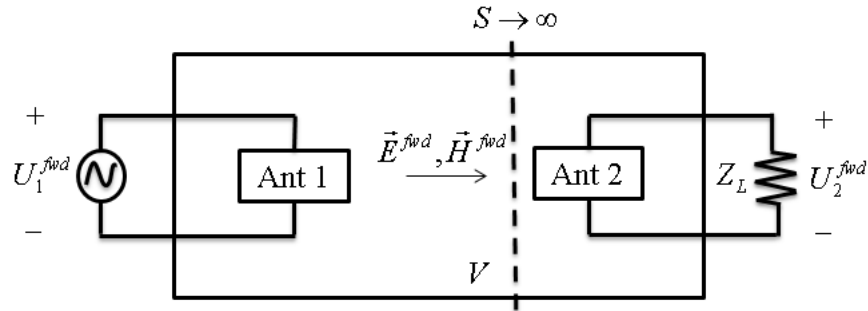
(a) The forward problem
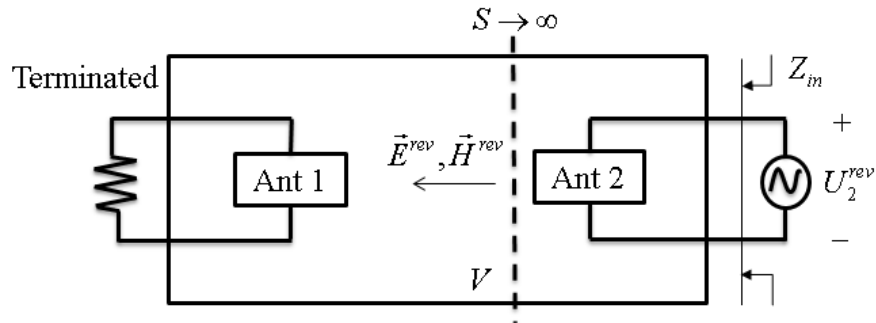
(b) The reverse problem

Figure 3.5. Coupling between two antennas with load

For any infinitely large surface S that separates the two sources, the reactions $\langle 1,2 \rangle$ and $\langle 2,1 \rangle$ can be calculated by (6) and (7). For these reactions, they can be represented by the integral of CC on the surface S as illustrated in (9) because of the reciprocity. They can also be expressed by the port voltages and the impedances. The following equation illustrates the detailed derivations.

$$\langle 1,2 \rangle = \iiint_V \left(\vec{E}_2^{\,fwd} \cdot \vec{J}_2^{\,rev} - \vec{H}_2^{\,fwd} \cdot \vec{M}_2^{\,rev} \right) dv'$$

$$= \iint_{S_2} \left(\vec{E}_2^{\,fwd} \cdot \vec{J}_2^{\,rev} + \vec{H}_2^{\,fwd} \cdot \vec{M}_2^{\,rev} \right) ds'$$

$$= I_2^{fwd} U_2^{rev} + I_2^{rev} U_2^{fwd}$$

$$= \left(\frac{1}{Z_{in}} + \frac{1}{Z_L} \right) U_2^{fwd} U_2^{rev} \tag{13}$$

In Equation (13), S_2 is the overall surface of the antenna 2, Z_L is the load impedance on port 2 in the forward problem, and Z_{in} represents the input impedance of port 2 in the reverse problem. Therefore, the coupled voltage on the load can be expressed by the surface integral of CC:

$$U_2^{fwd} = \frac{Z_{in} Z_L}{U_2^{rev} (Z_{in} + Z_L)} \times \iint_{S \to \infty} CC ds' \tag{14}$$

Note that U_2^{fwd} and U_2^{rev} are the total voltages, (14) can be simplified by replacing U_2^{rev} with the incident voltage $U_{2\_i}^{rev}$ [15]. Furthermore, both the characteristic impedance of the port Z_o and the load impedance Z_L are 50 ohms. Thus,

$$U_2^{fwd} = \frac{Z_{in} Z_L}{(1+\Gamma) U_{2\_i}^{rev} (Z_{in} + Z_L)} \times \iint_S CC ds'$$

$$= \frac{Z_{in} Z_L}{\left(1 + \dfrac{Z_{in} - Z_o}{Z_{in} + Z_o} \right) U_{2\_i}^{rev} (Z_{in} + Z_L)} \times \iint_S CC ds' \tag{15}$$

$$= \frac{Z_L}{2 U_{2\_i}^{rev}} \times \iint_S CC ds'$$

The power provided in the reverse problem is calculated by

$$P_{rev} = \frac{(U_{2\_i}^{rev})^2}{2 Z_o} \tag{16}$$

In the forward problem, the coupled power P_c on the load can be calculated from the following equation.

$$P_c = \frac{(U_2^{fwd})^2}{2Z_L} = \frac{\left(\frac{Z_L}{2U_{2\_i}^{rev}} \times \iint_S CCds'\right)^2}{2Z_L} = \frac{1}{16P_{rev}}\left(\iint_S CCds'\right)^2 \qquad (17)$$
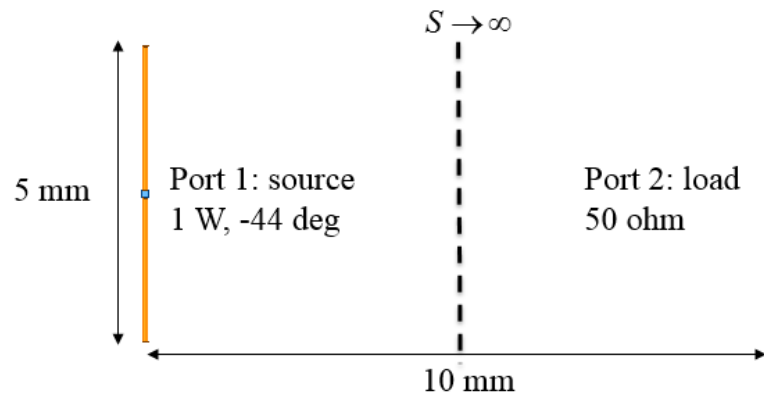
(a) The forward problem
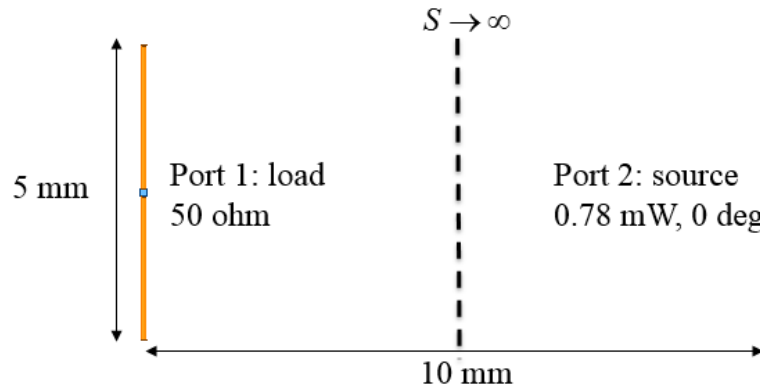
(b) The reverse problem

Figure 3.6. Two half-wavelength dipole antennas with loads

If the reverse power P_{rev} is set to be $1/16$ of the coupled power P_c in the forward problem, the coupled power on the load will be equal to the surface integral of CC:

$$P_c = \iint\limits_{S \to \infty} CC ds'$$ (18)

To validate (18), two terminated ports were assigned to the dipole antennas in the model shown in Figure 3.6. Following the phase adjustment in Figure 3.3, when the phase of excitation in the forward problem was -44 degrees, the coupled voltage on the 50 ohm load was $U_2^{fwd} = 1.12$ V, the coupled power was $P_c = 12.54$ mW. In the reverse problem, the provided power was set to be 0.78 mW, which satisfies $P_{rev} = P_c /16$. The coupling coefficient was then calculated. Figure 3.7 shows the real part of the CC on the large plane in the middle of the two antennas. Its surface integral was 12.54 mW, which was equal to the coupled power.
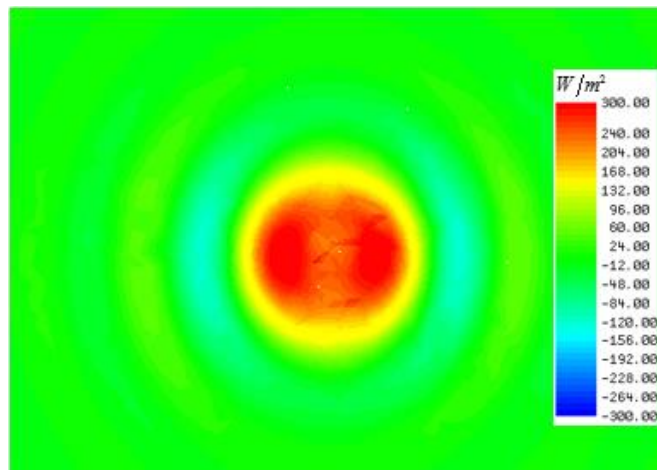
Figure 3.7. The real part of CC on a large plane

Comparing Figure 3.4 and Figure 3.7 shows that the CC distribution patterns are the same. The only difference is their scales. Because the geometries and locations of antennas in two examples are the same, the coupling mechanism does not change.

Excitation differences only affect the coupling strengths. In sum, for the case with a load, the coupled power on the load is equal to the surface integral of CC when the reverse power is assigned to be 1 / 16 of the coupled power in the forward problem. In this situation, the CC has the meaning of coupling power density. Similar to the current density, the coupling coefficients have different values on the cross section planes with different normal vectors.

3.3. DIPOLE-MOMENT BASED SYSTEM

According to the dipole-moment based source reconstruction, the finite sized noise source can be replaced by equivalent dipole moments. The system with equivalent dipole moments is commonly used in EMI problems. For dipole moments, it is meaningless to talk about the coupled power on it. Previous derivations and illustrations for the two-port networks cannot be directly used in the dipole-moment based system. Thus, the physical insight of the surface integral of CC in the dipole-moment based system need to be determined.

As shown in Figure 3.8, there are two sets of dipole moments represented in scalar form. In the forward problem, a set of dipole-moments locates at position 1. In the reverse problem, another set of dipole-moments locates at position 2. Using the definition of infinitesimal dipole-moment, the volume integral of current density can be replaced by the dipole-moments, respectively. The new relationship is shown as below.

$$
\begin{aligned}
& E_{1x}^{rev} P_{1x} + E_{1y}^{rev} P_{1y} + E_{1z}^{rev} P_{1z} - H_{1x}^{rev} M_{1x} - H_{1y}^{rev} M_{1y} - H_{1z}^{rev} M_{1z} \\
& = E_{2x}^{fwd} P_{2x} + E_{2y}^{fwd} P_{2y} + E_{2z}^{fwd} P_{2z} - H_{2x}^{fwd} M_{2x} - H_{2y}^{fwd} M_{2y} - H_{2z}^{fwd} M_{2z} \\
& = \iint_{S \to \infty} CC ds'
\end{aligned} \tag{19}
$$

$S \to \infty$

(a) The forward problem

$S \to \infty$
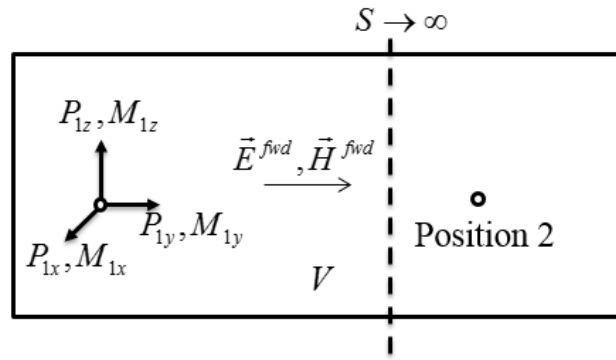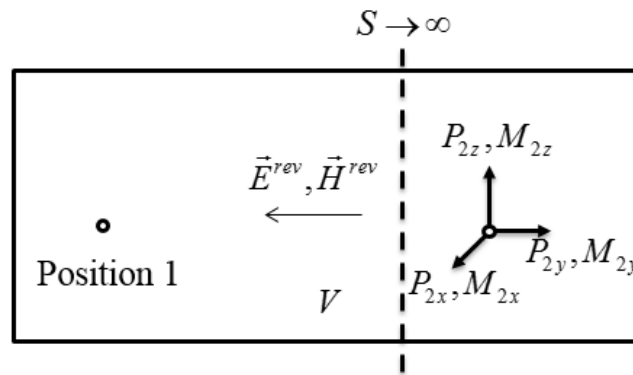
(b) The reverse problem

Figure 3.8. Dipole-moment based system

If there is only one type of dipole moment, the relationship given by reciprocity can be largely simplified. For example, as shown in Figure 3.9, the sources are a Pz dipole at position 1 in the forward problem and a Pz dipole at position 2 in the reverse problems. After phase adjustment, the coupled field component $E_{2z}^{fwd} = 1.862 \times 10^6 V / m$. In the reverse problem, $P_{2z} = 1 Am$. The real part of CC on the infinite surface S is shown in Figure 3.10. The surface integral of CC is $1.862 \times 10^6 W$ which is equivalent to the production of E_{2z}^{fwd} and P_{2z}. If the unit dipole moment is used in reverse problem, the surface integral of CC represents the coupled field component in the forward problem.

$S \rightarrow \infty$

10 mm

E_{2z}^{fwd}

Position 2

$P_{1z} = -0.167 + j0.986 Am$

(a) The forward problem

$S \rightarrow \infty$

E_{1z}^{rev}

10 mm

Position 1

$P_{2z} = 1 Am$
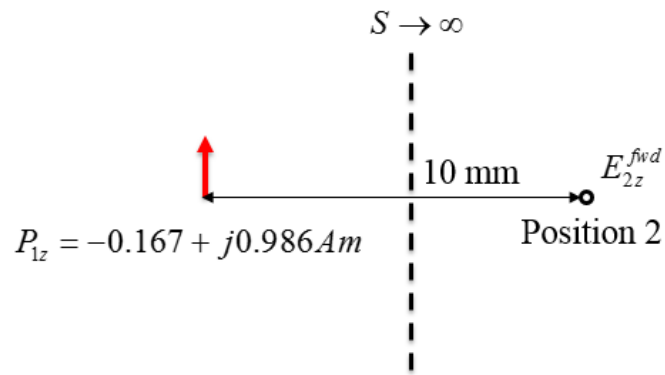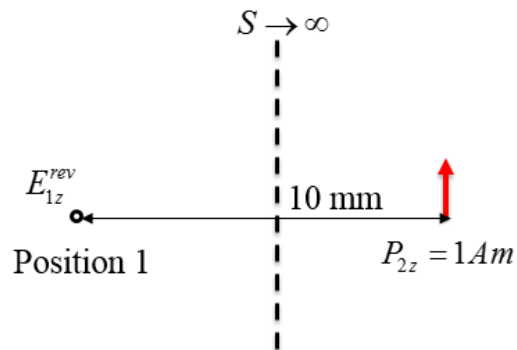
(b) The reverse problem

Figure 3.9. Two dipole moments

NamedExpr

5.00E+010
4.00E+010
3.40E+010
2.80E+010
2.20E+010
1.60E+010
1.00E+010
4.00E+009
-2.00E+009
-8.00E+009
-1.40E+010
-2.00E+010
-2.60E+010
-3.20E+010
-3.80E+010
-4.40E+010
-5.00E+010
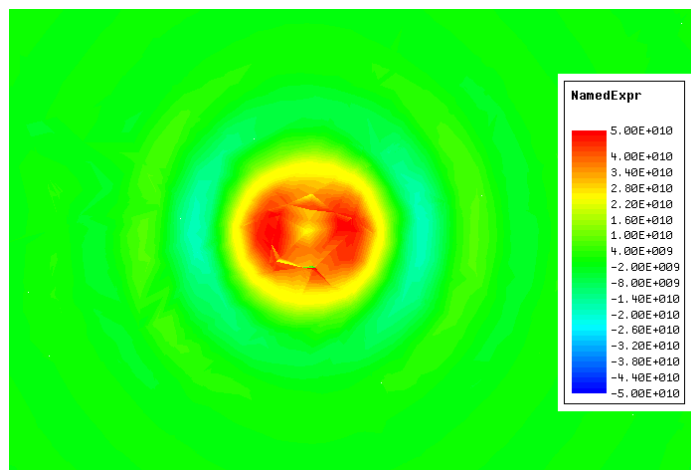
Figure 3.10. The real part of CC on a large plane

4. COUPLING PATH VISUALIZATION IN RECTANGULAR COORDINATES

4.1. VISUALIZATION METHOD

Another important feature of the coupling coefficient is its conservative property. For any closed surface that separates two sources, the surface integral of CC is constant. Figure 4.1 exhibits the special case that the closed surface is replaced by the large planes that extend to infinity.
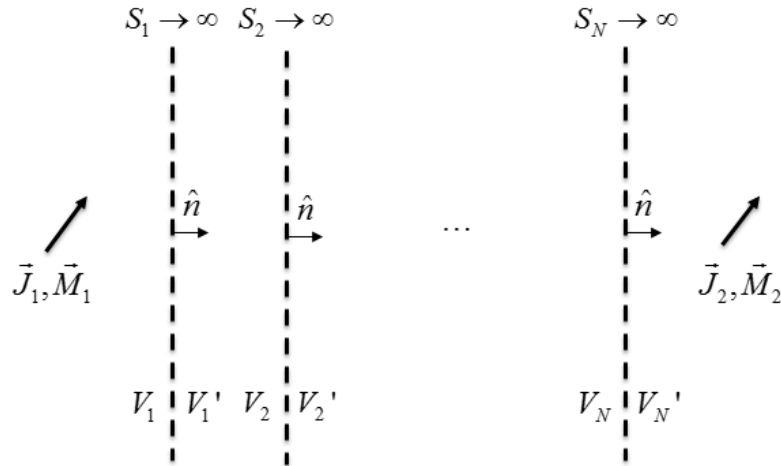
Figure 4.1. The conservative property of the surface integral of CC

These planes have the same unit normal vectors because these planes are in parallel. Therefore, the coupling coefficients on these planes have the same expressions. The conservative property is written as

$$\iint_{S_1} CCds' = \iint_{S_2} CCds' = ... = \iint_{S_N} CCds' \tag{20}$$

This property also makes the coupling coefficient comparable to the scalar current density. From last section, it has been known that CC has the meaning of coupling power density. The coupling power distribution on any cross section between two sources can be shown by plotting the scalar CC on the large plane. Furthermore, the 3D coupling paths can be visualized by plotting CC on all parallel planes between the sources. Based on this method, the coupling path can be visualized together with the simulation model in commercial simulation tools, for example, HFSS [16].

4.2. COUPLING BETWEEN TWO DIPOLE ANTENNAS

Before using the proposed visualization method on the terminated dipole antenna model in Figure 3.6, the magnitude of Poynting vector when antenna 1 was excited by 1 W source is plotted in Figure 4.2. It can be observed that the Poynting vector depicts radiation properties of the excited antenna rather than the coupling between two antennas.
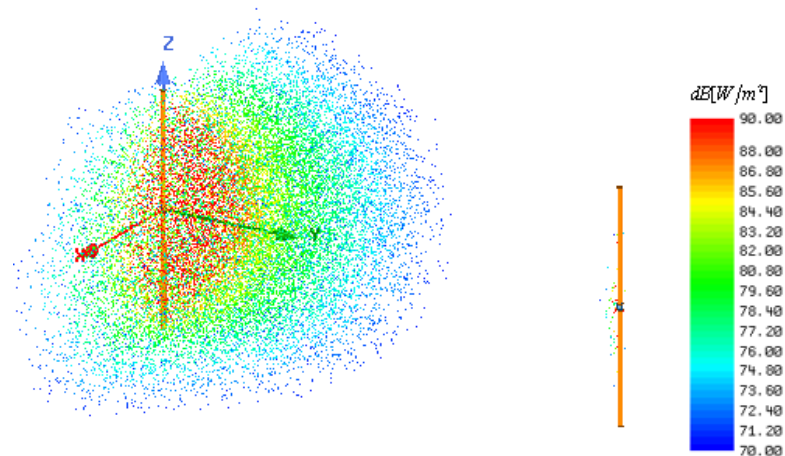
Figure 4.2. Plotting the magnitudes of Poynting vector

Therefore, the proposed method based on the coupling coefficient was applied. The parallel large planes were selected in the XZ domain. The common unit normal vector of these planes was $\hat{y}$. The 3D coupling path is shown in Figure 4.3 by plotting the real part of CC over the space between two antennas. For each XY plane between the antennas, the surface integral of CC was calculated to be 12.54 mW, which satisfied the conservative property.
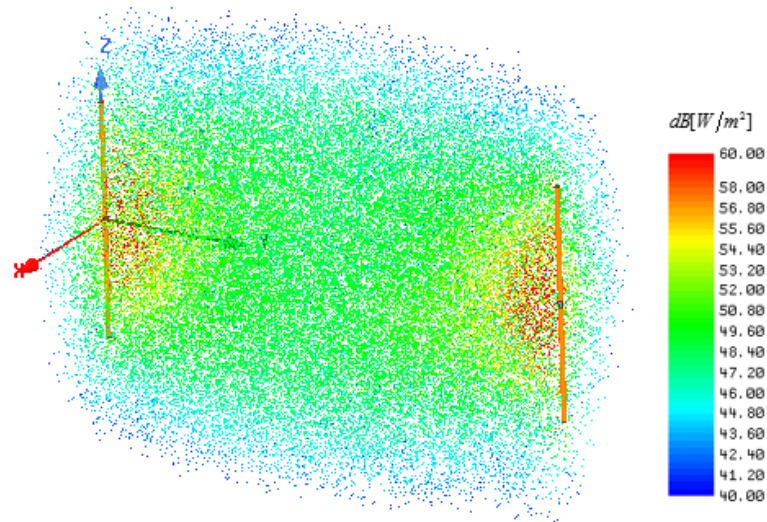
Figure 4.3. The 3D coupling path of two dipole antennas

For the same dipole antennas, a large PEC plate with five apertures was placed in between of them, as shown in Figure 4.4. The coupling path was different because of the added plate. As estimated, the coupling between two dipole antennas only took place through the apertures. If the plate has no apertures and is infinitely large, the coupling between two antennas will become zero. The five apertures shown in Figure 4.4 allow the coupling to exist. However, the coupled power on the load reduced to 0.32 mW.
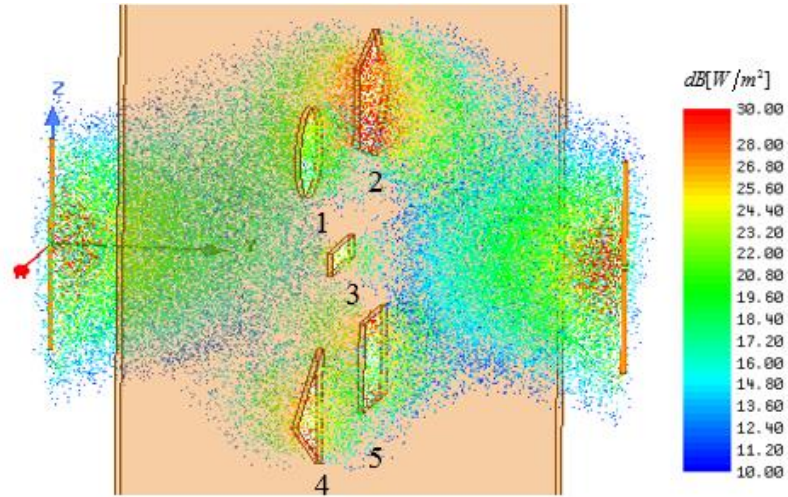
Figure 4.4. The 3D coupling paths that penetrating apertures

Furthermore, the coupling power ratio of these paths can be quantified. Figure 4.5 shows the real part of CC on the plate's surface. On PEC surface, the projections of cross production terms in the CC's definition (8) on the normal direction are zero because the tangential E-fields on PEC are zero. Therefore, the CC on PEC surface is zero while it is non-zero on the aperture surfaces. Let us designate five coupling paths in response to the five apertures. In Table 4.1, the surface integrals of CC and their ratio are listed in the second and the third columns.

For comparison, the integrals of the magnitude of Poynting vector and their ratio are also listed in the last two columns. From the coupling path of two dipole antennas, it is found that the coupling power density concentrates at the center, as shown in Figure 4.3. However, in the example shown in Figure 4.4, the dominated coupling path is no longer at the center. In fact, the path at the center contributed the least to the coupled power. Instead, the second aperture contributes the most to the coupling.
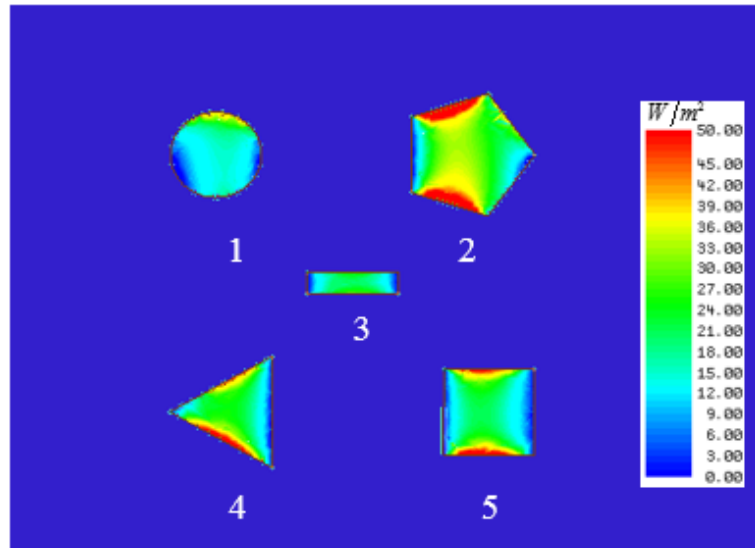
Figure 4.5. Quantification of the coupling path ratios

Table 4.1. Coupling path ratios

Path	Integral of CC [mW]	Ratio	Integral of P's magnitude [mW]	Ratio
1	0.04	12.3%	0.23	9.3%
2	0.14	43.8%	1.32	53.7%
3	0.01	4.2%	0.26	10.6%
4	0.06	17.8%	0.27	11.0%
5	0.07	21.9%	0.38	15.4%
Total	0.32	100%	2.46	100%

The total integral of Poynting vector magnitude is 2.46 mW which is much larger than the coupled power. Therefore, it is not correct to quantify the coupling ratios of different paths based on Poynting vector. Instead, the surface integral of CC should be used for coupling ratio quantification.

4.3. COUPLING IN RFI PROBLEMS

For the near-field situations, the coupling path visualization also works well. Figure 4.6 exhibits a typical RFI model contains a noise source and an embedded antenna on the DUT. Resonant frequency of the inverted-F antenna was designed to be 1.3 GHz. Let the noise source be a tangential magnetic dipole at the same frequency. The dipole was placed 1 mm above the ground plane.
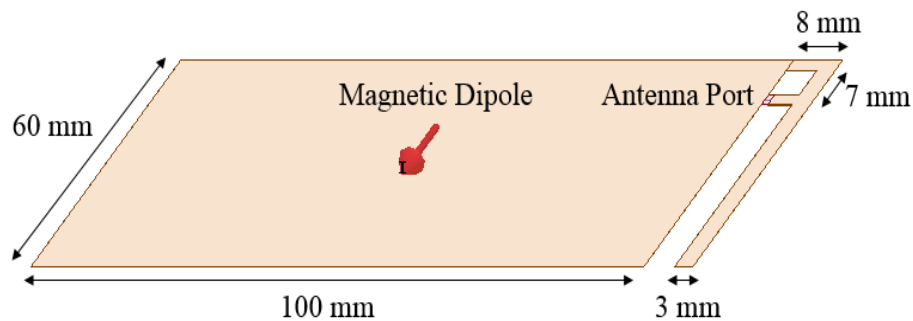
Figure 4.6. A typical RFI model in HFSS

In the forward problem, the magnitude and phase of the dipole were set to be 1 Vm and −65.78 degrees, respectively. The coupled voltage on the 50 ohm antenna port was then measured to be 2.19 V. The coupled power on the load was calculated to be 47.79 mW. In the reverse problem, the dipole strength was set as zero. The power provided on the antenna port was 2.99 mW, which was 1/16 of the forward coupled power. By using definition (8), the coupling coefficient over the entire space was calculated. Figure 4.7 shows the real part of CC on a large XY plane. The surface integral of CC on this plane was 47.53 mW, which was close to the forward coupled power with small numerical error.
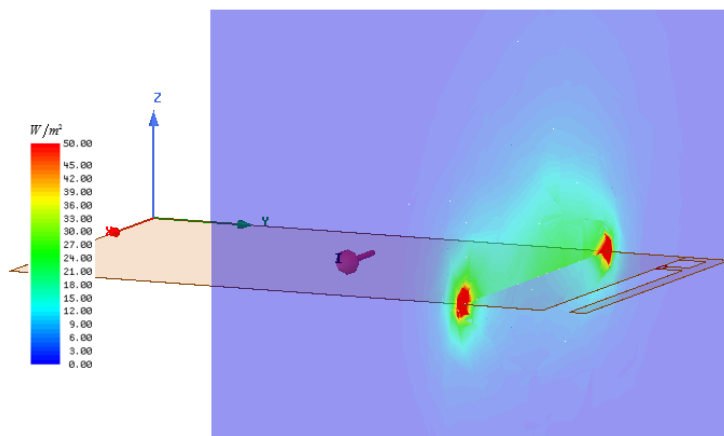
Figure 4.7. The real part of CC on a large cross section

From this cross section plane, two major coupling paths can be found. For the path on the left side and that on the right side, their coupling power ratios were calculated to be 46% and 54%, respectively. The 3D coupling path was visualized in Figure 4.8. The intuitive conclusion for this RFI model is that the majority coupling energy from the noise source to the victim antenna is flowing along the edge of the ground plane.
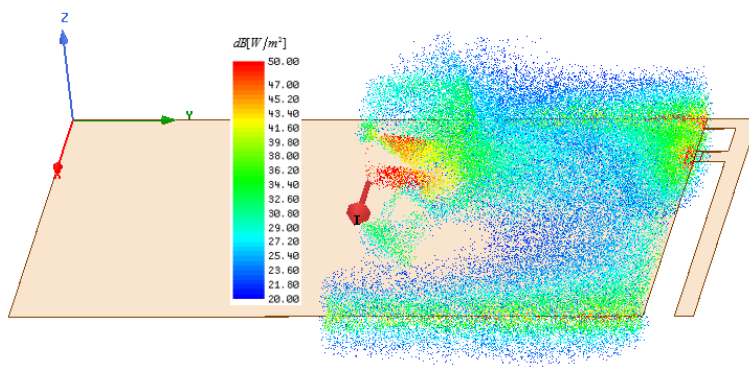
Figure 4.8. The coupling path visualization for the RFI model

5. COUPLING PATH VISUALIZATION IN SPHERICAL COORDINATES

In last section, the closed surfaces were selected as infinite planes which separates two sources. Therefore, the coupling paths between two sources can be visualized by plotting CC. However, the surface integral of CC becomes zero on the infinite plane that on one side of the sources. As shown in Figure 5.1, the surface S_{N+1} does not separate source 1 and source 2 and thus the defined CC is invalid on this plane. For the source 2 in Figure 5.1, the visualization method in rectangular coordinates can only exhibit the coupling path on the left side. In some cases, it is important to characterize the coupling path from all directions around the victim or aggressor but the method in last section cannot work. To solve this problem, CC is converted into spherical coordinates where the origin is set as the victim location or aggressor location.

$$\iint_{S_1} CCds' = \iint_{S_2} CCds' = \ldots = \iint_{S_N} CCds' \qquad \iint_{S_{N+1}} CCds' = 0$$

$$\ldots$$

$$S_1 \to \infty \quad S_2 \to \infty \qquad S_N \to \infty \qquad S_{N+1} \to \infty$$

$\hat{n} \qquad \hat{n} \qquad \ldots \qquad \hat{n} \qquad \hat{n}$

$\vec{J}_1, \vec{M}_1 \qquad\qquad\qquad\qquad \vec{J}_2, \vec{M}_2$

$V_1 \; V_1' \quad V_2 \; V_2' \qquad\qquad V_N \; V_N'$
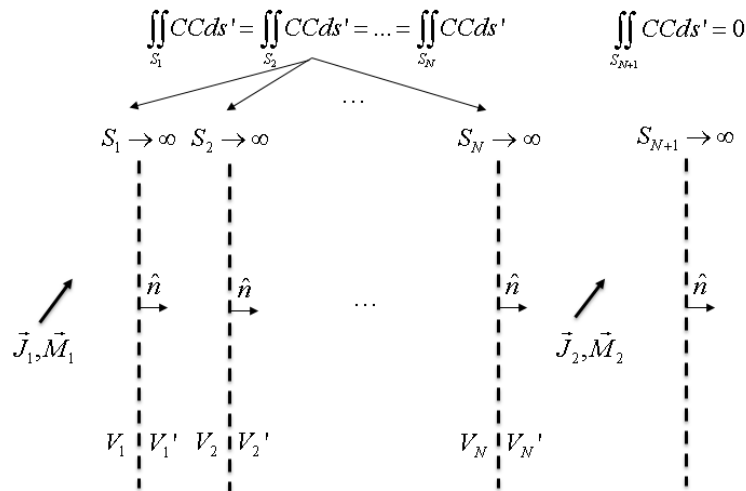
Figure 5.1. Limitation of using CC in rectangular coordinates

As shown in Figure 5.2, defining the victim location as origin point of the spherical coordinates, the closed surfaces are selected as the origin centered spherical surfaces that separates the aggressor and victim. The normal vector becomes $\hat{r}$. By plotting the CC in spherical coordinates, coupling path around the victim can be clearly visualized.
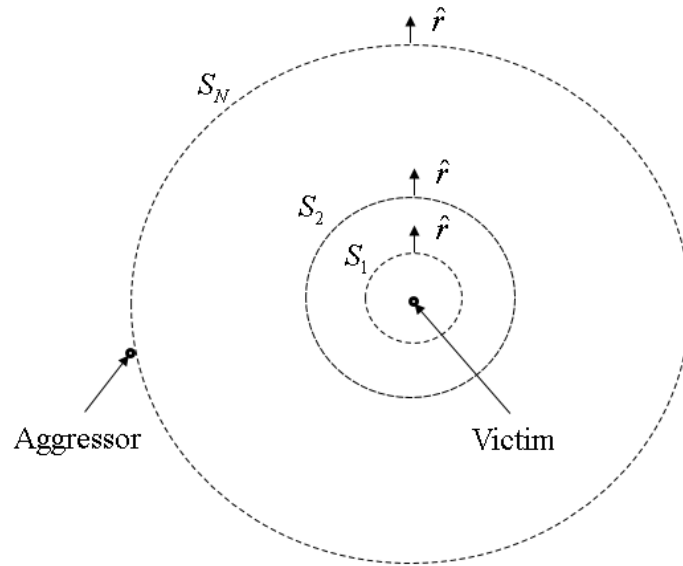
Figure 5.2. Using CC in spherical coordinates

6. APPLICATION IN AUTOMOTIVE IEMI

With the increasing use of electronics to control every aspect of modern automobiles, from engine management to driverless cars, intentional electromagnetic interference (IEMI) is a growing threat. The driverless car, for example, depends on electronics that detect roads, traffic, and any obstacles that suddenly emerge and then control engine accordingly. IEMI attack could disable them, possibly causing injuries or fatalities. Numerous investigations have been conducted on the disruptive and damaging effects of IEMI attacks on automobiles. In report [17], among 37 cars tested in an electromagnetic pulse (EMP) environment, three cars stopped at field strength of 30kV/m or above, twenty-five automobiles exhibited malfunctions, and electronics in the dashboard of one automobile were permanently damaged. In order to effectively protect against the risk of IEMI, it is required to understand the nature of attack at first. Several automotive IEMI experiments were conducted [18][19]. In this section, the effective automotive IEMI simulation model using dipole moment is proposed. Also, the coupling path visualization method is applied in the automotive IEMI simulation.

6.1. IEMI SOURCE MODELING

The IEMI source Replex HPEM-DMS-120KV is exhibited in Figure 6.1 [20]. The attack source uses a dipole-shape antenna as a radiator. The ideal waveform generated by this source is a damped sinusoidal wave. Its percentage bandwidth and band ratio satisfy the standard mesoband source specification for the IEMI experiments defined in the IEC 61000-4-36 [21].
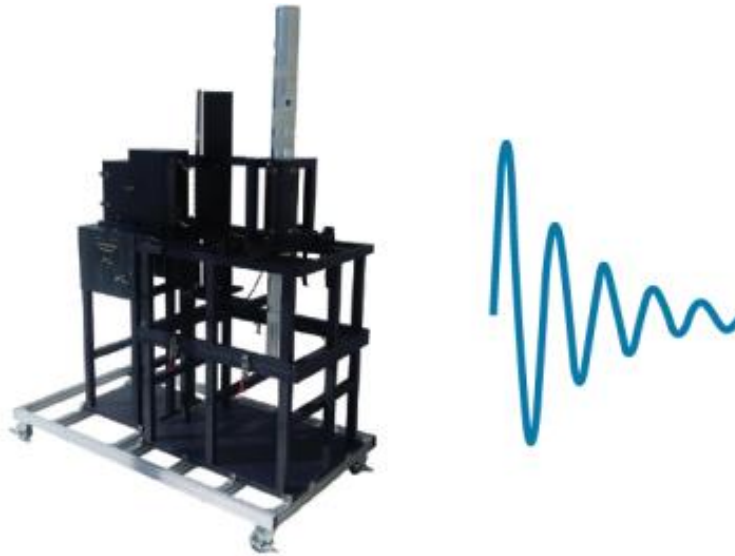
Figure 6.1. Standard mesoband source

Figure 6.2 shows the set-up for measuring the fields generated by the IEMI source. The measured fields were then used for source reconstruction. TEM sensor was used to measure the z component of E-field. High voltage attenuator and RF attenuator were connected to the TEM sensor in order to reduce the signal amplitudes to satisfy the input range of the electric-optic converter. For safety, the oscilloscope was placed far away from the measurement region, the long optical fiber was used to avoid the signal degradation and potential electromagnetic coupling to the wire. E/O converters were added on the two ends of the optical fiber.

The voltage measured by the oscilloscope can be converted to the electric field intensity after calibration. There are three columns of measurement points in parallel. For the center column points, their distances to the source varies from 3 m to 10 m with 1 m step.
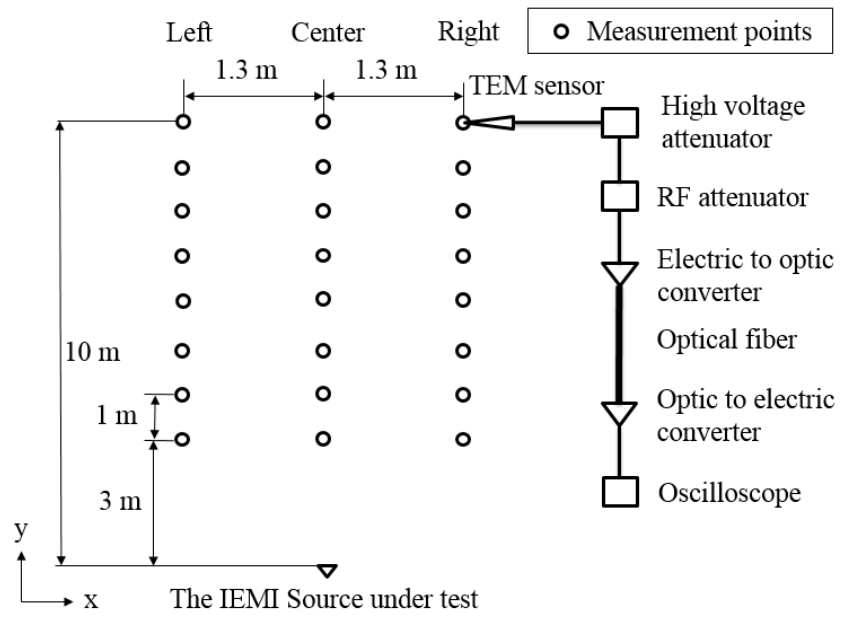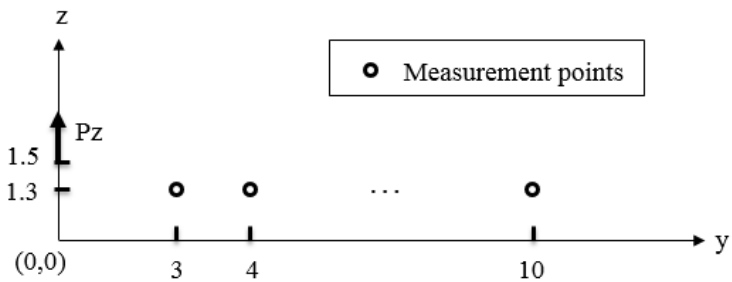
Figure 6.2. Measurement set-up for the IEMI source modeling

(a) Real measurement set-up

(b) Coordinate of source and measurement locations

Figure 6.3. Measurement set-up for the IEMI source modeling

Figure 6.3 (a) is a picture shows the real measurement set-up. Figure 6.3 (b) shows the coordinate of the source and measurement locations. The time-domain data was measured at each points. The source can generate 10 pulses in one second. For each measurement point, 30 pulses were recorded by the oscilloscope which was triggered by the rising edge. The proper one among 30 measured pulses will be used in the following calibration and source reconstruction.
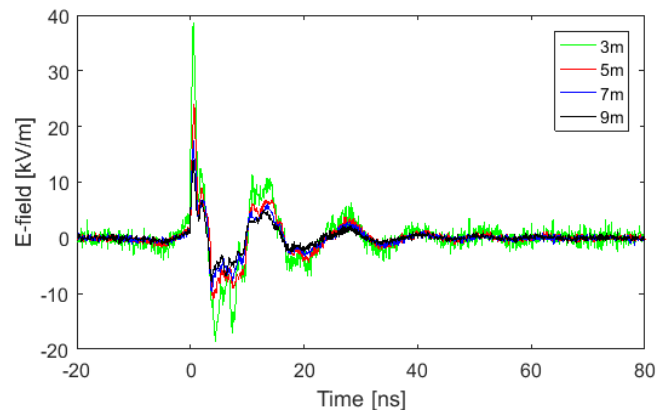
(a) Waveforms in the time domain
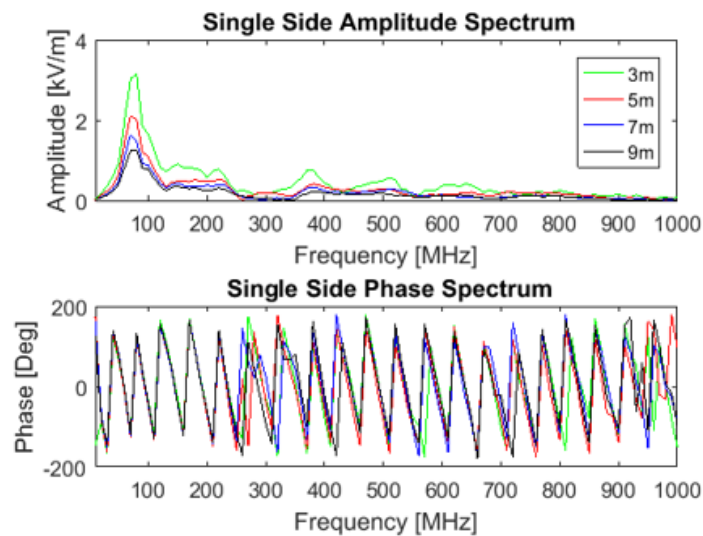
(b) Single side spectrums in the frequency domain

Figure 6.4. IEMI source measurement data

The measured raw data was converted to the field data by multiplying the transfer function. Figure 6.4 (a) shows the waveform of E_z at several measurement points in the center column. Figure 6.4 (b) shows the corresponding single side amplitude and phase spectrums. The fields at different distances are plotted on top of each other. The time delay caused by the propagation distance difference has been excluded. Therefore, the measured pulses start at the same time in Figure 6.4 (a). In the spectrum, they also have the same phases at the frequencies with significant amplitudes.

The far field boundary of the IEMI source can be estimated by:

$$R = \frac{2D^2}{\lambda} = \frac{2 \times 2^2 m^2}{3m} \simeq 2.67m \tag{21}$$

In Equation (21), D is the largest dimension of the antenna. λ is the wavelength of 100 MHz signal. When the distance to source is larger than 2.67 m, it will belong to the far field region. In far field, it is reasonable to replace the source by an ideal infinitesimal electric dipole. As shown in Figure 6.3 (b), the vertical electric dipole P_z is used to replace the IEMI source. The equivalent dipole is placed at $Z = 1.5$m, which is that same height of the center of the original source. The height of TEM sensor is 1.3 m. The data used for source reconstruction is E_z at the observation points in the center column. The rest geometry information is given by Figure 6.2.

According to the antenna theory, the transfer function between a dipole moment and its generated field can be calculated once the geometries and frequency are known [22]. For example, the E_z at the observation point (x, y, z) that generated by a dipole P_z can be calculated by:

$$E_z(x, y, z) = K_E[-\frac{x^2 + y^2}{r^2} g_1(r) + g_2(r)]P_z \qquad (22)$$

In Equation (22), r is the distance from the dipole to the observation point. K_E is related to the wave impedance η_0 and the propagation constant k_0:

$$K_E = -j\frac{k_0\eta_0}{4\pi} \qquad (23)$$

The $g_1(r)$ and $g_2(r)$ in (2) represent the following terms:

$$g_1(r) = \left[\frac{3}{(k_0r)^2} + j\frac{3}{k_0r} - 1\right]\frac{e^{-jk_0r}}{r}$$

$$g_2(r) = \left[\frac{2}{(k_0r)^2} + j\frac{2}{k_0r}\right]\frac{e^{-jk_0r}}{r} \qquad (24)$$

From (22) to (24), the transfer function is obtained. From the measurement results, we can also calculate the synchronized field components by

$$E_z^{3m} = \left|E_{z,measured}^{3m}\right|e^{j\phi_{3m}}$$

$$E_z^y = \left|E_{z,measured}^y\right|e^{j\phi_y}e^{-jk_0(y-3m)}, y = 4m, 5m, ..., 10m \qquad (25)$$

In Equation (25), $\left|E_{z,measured}^{3m}\right|$ represents the magnitude of the measured E_z component at 3m, ϕ_{3m} is the corresponding measured phase. In (5), the measured field at 3 m is used as reference. The fields at other locations are then modified by the phase term $e^{-jk_0(y-3m)}$. After using (25), the calculated E_z at different locations become the real time measurement results of a single excitation. With the synchronized fields and the transfer function, the equivalent source P_z can be calculated from (22). The matrix form of (22) is written as
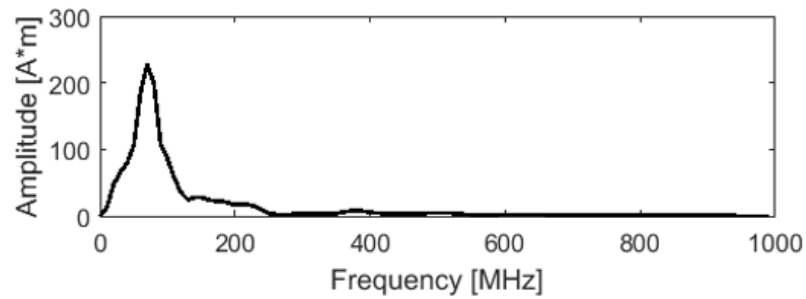
$$E_z = TF \cdot P_z \tag{26}$$

TF and E_Z are vectors defined by

$$TF = \left[TF^{3m}, TF^{4m}, ..., TF^{10m} \right]$$
$$E_z = \left[E_z^{3m}, E_z^{4m}, ..., E_z^{10m} \right] \tag{27}$$
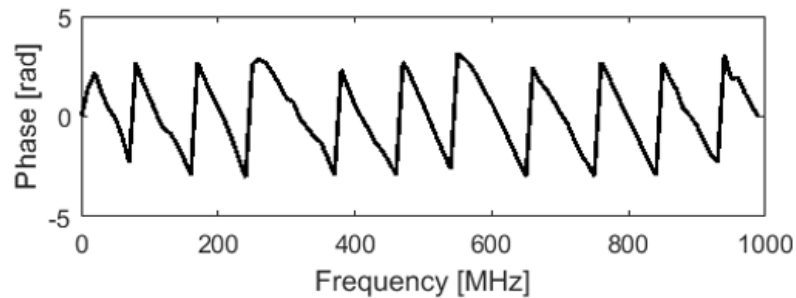
Since there are more than one observation points while only one unknown source, the least square method was used in solving the following equation [23]:

$$P_z = \left[TF \, ' TF \right]^{-1} TF \, ' E_z \tag{28}$$

Figure 6.5 shows the reconstructed 100 dipoles from 10 MHz to 1 GHz with the step of 10 MHz.


(a) Magnitudes

(b) Phases

Figure 6.5. The equivalent dipoles

Importing the reconstructed dipoles into the EMCoS [24], the fields at the observation points can be simulated. Figure 6.6 (a) and (b) exhibit the comparison of measurement results and those in simulation at the point that is located in the center column and 3 m away from the source. Moreover, Figure 6.7 shows the comparison of the peak values in the time domain waveforms. The comparison for the right column points is the same as Figure 6.7 (b). For the observation points in the left or right columns, different distances to the source correspond to different azimuth angles. Therefore, the comparison in Figure 6.7 (b) suggests that the equivalent dipoles characterized the radiation pattern of the original IEMI source.
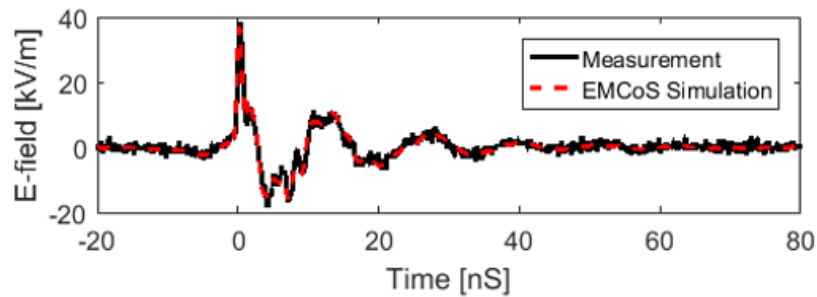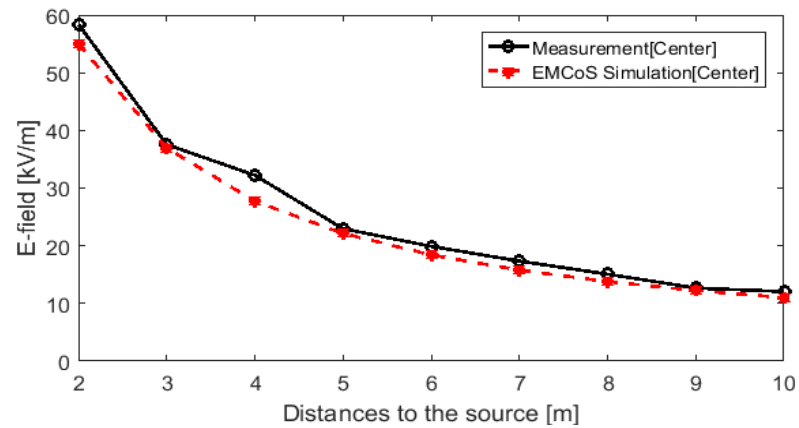

(a) Waveforms in the time domain
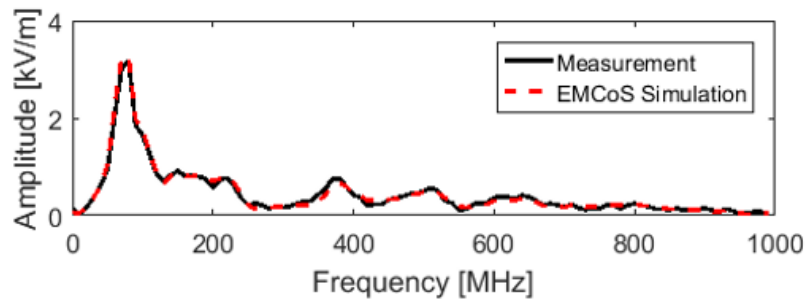
(b) Single side amplitude spectrums in the frequency domain

Figure 6.6. E-field comparison at the center column, 3m

In sum, the perfect matches in Figure 6.6 and Figure 6.7 indicate that the equivalent dipole reconstruction based on the least square method is suitable for the high power source modeling.

(a) Maximum values comparisons for the center column
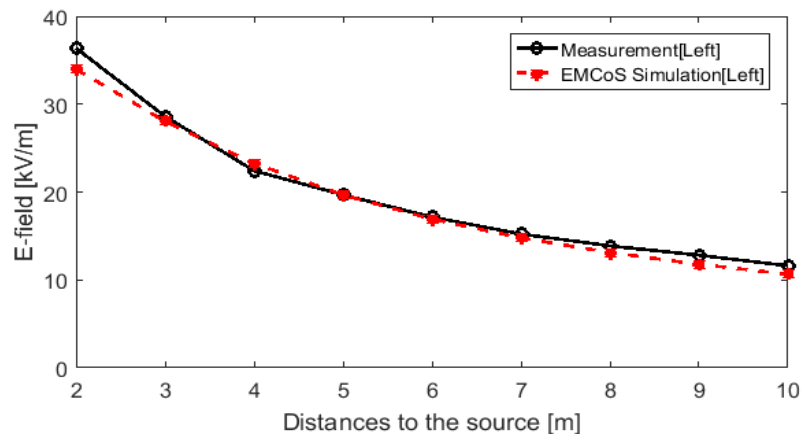
(b) Maximum values comparisons for the left column

Figure 6.7. The comparisons of the maximum values in the waveform

6.2. COUPLING PATH VISUALIZATION FOR IEMI SIMULATION

An IEMI experiment on a car was conducted using the same attack source as shown in Figure 6.8. Besides recording the behaviors of the car under the IEMI environment, the

vertical E-field inside the car were measured. D-dot sensor was used to measure the E-field component inside the car because of its small size. For example, the D-dot sensor was place close to the pedal. Thus, the E_z around the pedal was measured in the experiment.

Figure 6.8. IEMI experiment for car

Figure 6.9 illustrates the simulation model using the equivalent source. A field probe was added in the simulation model to obtain the field results in simulation.
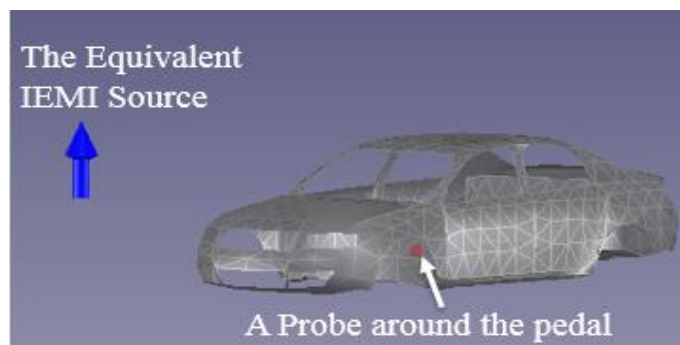

Figure 6.9. Illustration of the simulation model

Figure 6.10 shows the comparison of vertical E-field component in the experiment and that in the corresponding simulation when the source was placed 3m in front of the car. The small differences may be caused by the inaccuracy of the automotive model. Besides, potential multi-reflections between the source and the car was ignored in the simulation. The agreement of measurement and simulation indicates that the IEMI simulation model using the equivalent dipole moment is reliable.
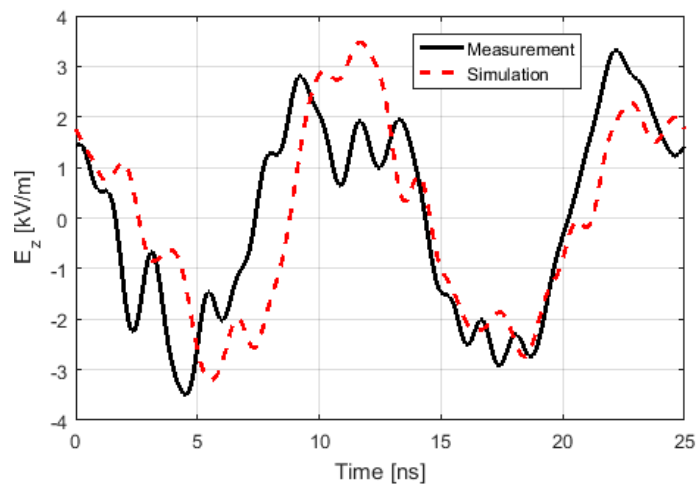
(a) Waveform of Ez in the time domain
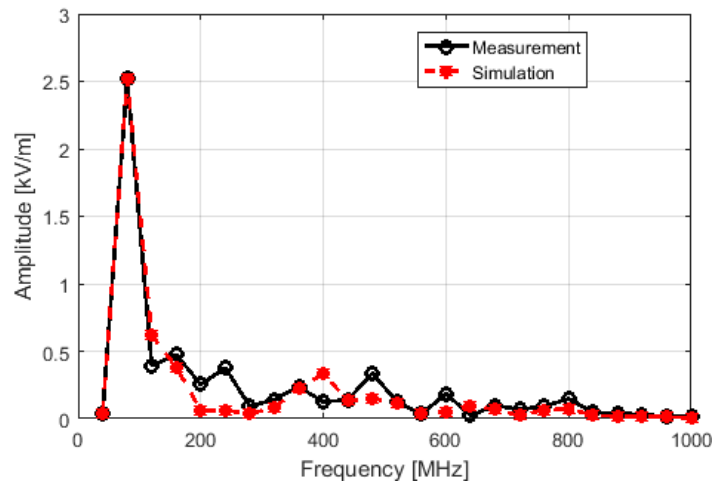
(b) Single side amplitude spectrum of Ez in the frequency domain

Figure 6.10. Comparison when the source is 3m in front of the car

For visualizing the coupling path, the forward and reverse simulations are done as shown in Figure 6.11.

(a) The forward simulation model

(b) The reverse simulation model
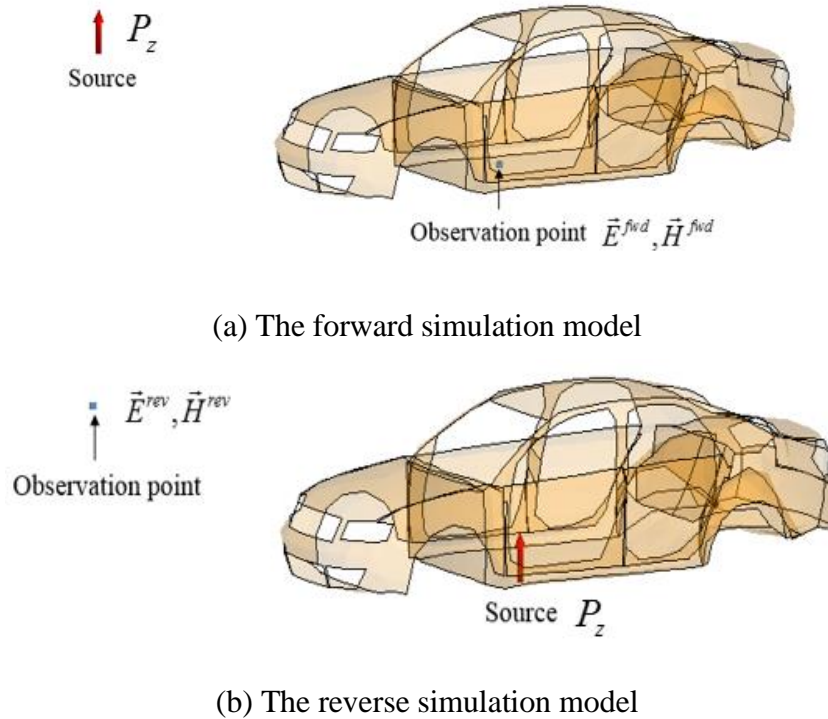
Figure 6.11. Simulation models based on the reciprocity theorem
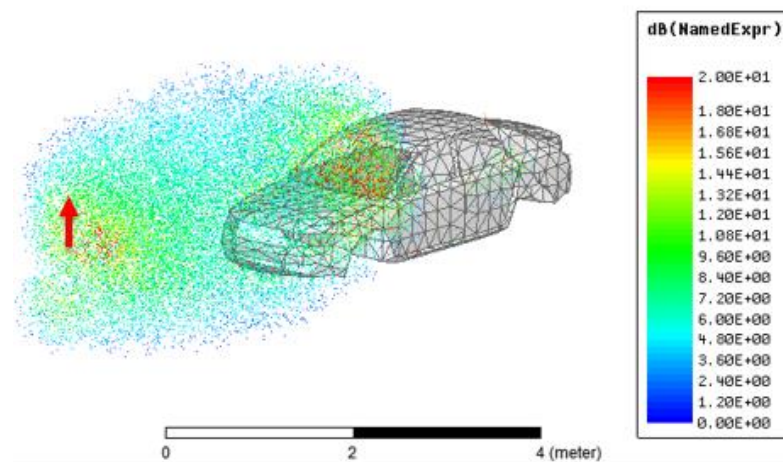
Figure 6.12. Coupling path when IEMI source is located in front of the car

Calculating and plotting CC in spherical coordinates where the origin is set at the pedal. The 3D coupling path at 100 MHz is shown in Figure 6.12. It can be observed that major coupling path passes through the front window of the car. For the IEMI source located on the left side of the car, the coupling path is also visualized in Figure 6.13. There are two major coupling paths: one is from the left side window and another is from the narrow gap under the front door.
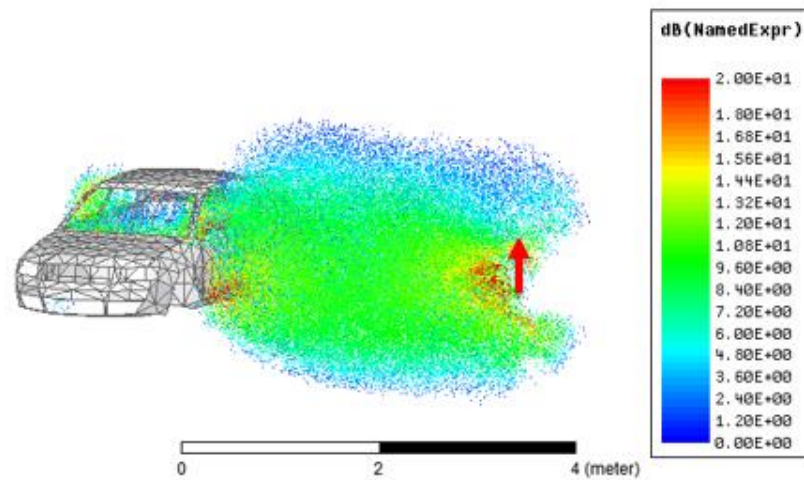
Figure 6.13. Coupling path when IEMI source is located on left side of the car

7. CONCLUSION

The proposed method can visualize a 3D coupling path by plotting the coupling coefficient over the space. It is derived from Maxwell's equation and has clear physical meaning. For example, the properly calculated coupling coefficient represents the coupling power density. Moreover, the visualization method has good compatibility with commercial simulation tools because the coupling coefficient can be conveniently calculated with their embedded field calculators. Since the coupling coefficient can be plotted on top of the simulation models, it is helpful for EMC engineers to identify and quantify the coupling path. The proposed method has been applied in both rectangular coordinates and spherical coordinates. Several examples has been used to illustrate the coupling path visualization method. Especially, the coupling path visualization for the automotive IEMI is detailed discussed.

BIBLIOGRAPHY

[1]   C. R. Paul, "Introduction to Electromagnetic Compatibility," 2nd ed. Hoboken, NJ, USA: Wiley, 2006.

[2]   S. Yang, P. Maheshwari, V. Khilkevich and D. J. Pommerenke, "Coupling path visualization using a movable scatterer," 2014 IEEE International Symposium on Electromagnetic Compatibility (EMC), Raleigh, NC, 2014, pp. 707-711.

[3]   T. Kurner, D. J. Cichon, and W. Wiesbeck, "Concepts and results for 3D digital terrain-based wave propagation models: An overview," IEEE J. Select. Areas Commun., vol. 11, no. 7, pp. 1002–1012, Sep. 1993.

[4]   V. Degli-Esposti, D. Guiducci, A. de'Marsi, P. Azzi, and F. Fuschini, "An advanced field predictionmodel including diffuse scattering," IEEE Trans. Antenna Propag., vol. 52, no. 7, pp. 1717–1728, Jul. 2004.

[5]   H. Li, V. V. Khilkevich, and D. Pommerenke, "Identification and visualization of coupling paths—Part I: Energy parcel and its trajectory," IEEE Trans. Electromagn. Compat., vol. 56, no. 3, pp. 622–629, Jun. 2014.

[6]   H. Li, V. V. Khilkevich, and D. Pommerenke, "Identification and visualization of coupling paths—Part II: Practical application," IEEE Trans. Electromagn. Compat., vol. 56, no. 3, pp. 630–637, Jun. 2014.

[7]   V. H. Rumsey, "Reaction concept in electromagnetic theory," Phys. Rev., vol. 94, no. 6, pp. 1483–1491, 1954.

[8]   J. H. Richmond, "A reaction theorem and its application to antenna impedance calculations," IRE Trans. Antennas Propag., vol. 9, no. 6, pp. 515–520, 1961.

[9]   J. Malmström, H. Holter and B. L. G. Jonsson, "On Mutual Coupling and Coupling Paths Between Antennas Using the Reaction Theorem," IEEE Trans. Electromagn. Compat., vol. 60, no. 6, pp. 2037-2040, Dec. 2018.

[10]   J.R.Carson, "Reciprocal Theorems in Radio Communication," Proc. IRE, vol. 17, pp. 952 − 956; June, 1929.

[11]   C. A. Balanis, Advanced Engineering Electromagnetics. Hoboken, NJ, USA: Wiley, 1989.

[12]   L. Sangsu, Y. Zhong, Q. Huang, T. Enomoto, S. Seto, K. Araki, J. Fan, and C. Hwang. "Analytical Intra-system EMI Model Using Dipole Moments and Reciprocity." Proc. IEEE Asia-Pac. Electromagn. Compat. Symp, 2018.

[13]   J. Pan, H. Wang, X. Gao, C. Hwang, E. Song, H. Park and J. Fan, "Radio-Frequency Interference Estimation Using Equivalent Dipole-Moment Models and Decomposition Methd Based on Reciprocity," IEEE Trans. Electromagn. Compat., vol. 58, no.1,pp. 75-84, Feb. 2016.

[14]   Q. Huang, F. Zhang, T. Enomoto, J. Maeshima, K. Araki, and C. Hwang, "Physics-based dipole moment source reconstruction for RFI on a practical cellphone," IEEE Trans. Electromagn. Compat., vol. 59, no. 6, pp. 1693–1700, Dec. 2017.

[15]   Q. Huang, T. Enomoto, S. Seto, K. Araki, J. Fan, and C. Hwang, "Efficient RFI Estimation and Mitigation using Dipole Moment Based Reciprocity" submitted to IEEE Transactions on EMC.

[16]   HFSS, ver. 18, Ansoft Corp., Pittsburgh, PA, USA, 2011. [Online]. Available: http://www.ansoft.com/.

[17]   Critical National Infrastructures, "Report of the Commission to Assess the Threat to the United States from Electromagnetic Pulse (EMP) Attack," 2004

[18]   M. Bäckström, "HPM testing of a Car: A Representative Example of the Susceptibility of Civil Systems", 13th International Zurich Symposium Supplement, February 1999, pp. 189-190.

[19]   Sabath, F., "What can be learned from documented Intentional Electromagnetic Interference (IEMI) attacks?" 2011 XXXth URSI General Assembly and Scientific Symposium, pp.1-4, 13-20 Aug. 2011.

[20]   Replex HPEM-DMS-120KV. Available: http://www.replex.co.kr/.

[21]   IEC 61000-4-36. Available: https://www.iec.ch/.

[22]   P.Wilson, "On correlating TEM cell and OATS emission measurements," IEEE Trans. Electromagn. Compat., vol. 37, no. 1, pp. 1–16, Feb. 1995.

[23]   M. Burger and J. Repisky, "Problems of linear least square regression and approaches to handle them," in Proc. 1st Virtual Int. Conf. Adv. Res. Sci. Areas, Dec. 2012, pp. 3–7.

[24]   EMCoS (2018). Available: https://www.emcos.com/.

VITA

Yang Zhong received his Bachelor of Engineering degree in Optoelectronic Information Science and Engineering from Huazhong University of Science and Technology, China in June 2017. He worked on Electromagnetic Interference in the EMC laboratory from 2017 to 2019. He received the Master of Science degree in Electrical Engineering from Missouri University of Science and Technology, USA in May 2019.